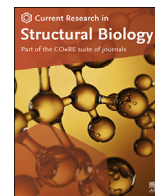


Contents lists available at [ScienceDirect](https://www.sciencedirect.com)

Current Research in Structural Biology

journal homepage: www.journals.elsevier.com/current-research-in-structural-biology

Insight into the nucleoside transport and inhibition of human ENT1

Zhixiang Wu^{a,1}, Zhongjie Han^{a,1}, Wenxue Zhou^a, Xiaohan Sun^a, Lei Chen^a, Shuang Yang^a, Jianping Hu^{b,**}, Chunhua Li^{a,*}^a Faculty of Environmental and Life Sciences, Beijing University of Technology, Beijing, China^b Key Laboratory of Medicinal and Edible Plants Resources, Development of Sichuan Education Department, School of Pharmacy, Chengdu University, Chengdu, China

ARTICLE INFO

Handling Editor: Natalie Strynadka

Keywords:

hENT1
Nucleoside transport
Adenosine
Dilazep
Inhibition mechanism

ABSTRACT

The human equilibrative nucleoside transporter 1 (hENT1) is an effective controller of adenosine signaling by regulating its extracellular and intracellular concentration, and has become a solid drug target of clinical used adenosine reuptake inhibitors (AdoRIs). Currently, the mechanisms of adenosine transport and inhibition for hENT1 remain unclear, which greatly limits the in-depth understanding of its inner workings as well as the development of novel inhibitors. In this work, the dynamic details of hENT1 underlie adenosine transport and the inhibition mechanism of the non-nucleoside AdoRIs dilazep both were investigated by comparative long-time unbiased molecular dynamics simulations. The calculation results show that the conformational transitions of hENT1 from the outward open to metastable occluded state are mainly driven by TM1, TM2, TM7 and TM9. One of the trimethoxyphenyl rings in dilazep serves as the adenosyl moiety of the endogenous adenosine substrate to competitively occupy the orthosteric site of hENT1. Due to extensive and various VDW interactions with N30, M33, M84, P308 and F334, the other trimethoxyphenyl ring is stuck in the opportunistic site near the extracellular side preventing the complete occlusion of thin gate simultaneously. Obviously, dilazep shows significant inhibitory activity by disrupting the local induce-fit action in substrate binding cavity and blocking the transport cycle of whole protein. This study not only reveals the nucleoside transport mechanism by hENT1 at atomic level, but also provides structural guidance for the subsequent design of novel non-nucleoside AdoRIs with enhanced pharmacologic properties.

1. Introduction

Nucleosides are the main components of nucleic acids and play critical roles in human metabolism, physiology and pharmacology (Wright and Lee, 2020). As important salvage metabolites, nucleosides can be readily converted to nucleotides via phosphorylation, providing raw materials for nucleic acid synthesis (Van Rompay et al., 2000; Yegutkin, 2014). Nucleotide biosynthesis is an energy intensive process that uses multiple metabolic pathways across different cell compartments and several sources of carbon and nitrogen (Lane and Fan, 2015). Although most proliferating cells (such as bone marrow cells) synthesize nucleotides and nucleic acids *de novo*, cells may also transport nucleosides from the extracellular environment (Downie et al., 2008). Owing to the hydrophilic nature of nucleosides, specialized transport systems are required to facilitate their penetration through plasma membrane and

some organellar membranes. Thus, nucleoside transport systems play key roles in many aspects of physiological and pathological regulation of living organisms. Moreover, nucleoside transport systems are directly responsible for the absorption, delivery, metabolism, and excretion (ADME) of some common nucleoside analogue drugs, such as ribavirin, remdesivir, penciclovir, gemcitabine, azidothymidine, etc (Seley-Radtke and Yates, 2018; Yates and Seley-Radtke, 2019). Some of them have already demonstrated early potential in the treatment of novel coronavirus disease 2019 (COVID-19) (Wang et al., 2020; Sheahan et al., 2020; Grein et al., 2020).

In mammalian cells, nucleoside transporters are classified into two major genetically distinct protein families: sodium-dependent concentrative nucleoside transporters (CNTs) corresponding to human SLC28 family and sodium-independent equilibrative nucleoside transporters (ENTs) corresponding to the SLC29 family (Young et al., 2013). Three

* Corresponding author. Faculty of Environmental and Life Sciences, Beijing University of Technology, Beijing, 100124, China.

** Corresponding author. Key Laboratory of Medicinal and Edible Plants Resources, Development of Sichuan Education Department, School of Pharmacy, Chengdu University, Chengdu, 610106, China.

E-mail addresses: hjpedu@163.com (J. Hu), chunhuali@bjut.edu.cn (C. Li).¹ These authors contributed equally to this work.<https://doi.org/10.1016/j.crstbi.2022.05.005>

Received 15 March 2022; Received in revised form 2 May 2022; Accepted 18 May 2022

2665-928X/© 2022 The Authors. Published by Elsevier B.V. This is an open access article under the CC BY-NC-ND license (<http://creativecommons.org/licenses/by-nc-nd/4.0/>).

human CNT isoforms (hCNT1-3) are respectively encoded by human SLC28A1, SLC28A2 and SLC28A3, while SLC29A1, SLC29A2, SLC29A3, SLC29A4 genomes are responsible for encoding four human ENT isoforms (*i.e.*, hENT1-4). The spatial expression of CNTs and ENTs is different in many human tissue types, indicating complementary and coordinated functional characteristics (Govindarajan et al., 2007). According to phylogenetic analysis, ENT family has a long evolutionary history, and its members are confined to eukaryotes, except for a special virus-derived subtype (see Fig. S1). Among them, hENT1 has attracted increasing attention of pharmaceutical chemists due to its wide distribution, especial its crucial role in adenosine and nucleoside analog drug transport in the human body (Young et al., 2008; Griffiths et al., 1997; Molina-Arcas et al., 2009).

At present, the nucleoside transport mechanism of CNTs has been extensively studied (Krishnamurthy et al., 2009; Jardetzky, 1966; Yamashita et al., 2005; Hirschi et al., 2017; Faham et al., 2008; Weyand et al., 2008). Based on a series of structural and computational biology studies on CNT, a multistep elevator-like nucleoside transport mechanism has been widely recognized (Hirschi et al., 2017; Duan et al., 2021). Although many functional analyses of ENTs have been performed experimentally, more structural advancements and conformational transition details still need to be further explored (Downie et al., 2008; Huang et al., 2017; Sundaram et al., 2001; Engel et al., 2004; Arastu-Kapur et al., 2003, 2005). It is worth mentioning that hENT1 is an effective controller of adenosine signaling by regulating extracellular and intracellular concentration, which has become a drug target of adenosine reuptake inhibitors (AdoRIs)—commonly used clinical vasodilators and antithrombotic drugs for cardiopathy, renal disease and hypertension (Nam et al., 2013; Nam et al., 2012; Asatryan et al., 2011; Ruby C et al., 2010; Lindberg et al., 2015). The lack of in-depth understanding of hENT1 inhibition mechanism by AdoRIs greatly restricts the development of such novel inhibitors.

Until recent years, Wright et al. constructed a functional variant of hENT1 with high biochemical stability, and also determined two crystal structures in complex with the non-nucleoside AdoRIs dilazep (a clinically used vasodilator) and the adenosine analog AdoRIs NBMPR (Wright and Lee, 2019). These two static outward-facing structures have laid the foundation for revealing hENT1-mediated adenosine transport and its inhibition mechanism. However, the nucleoside transport facilitated by hENT1 is a dynamic and continuous process; the structure of hENT1 in complex with the endogenous adenosine substrate is still unknown; there are few studies on the inhibition mechanism of AdoRIs at the atomic scale. Therefore, the following meaningful scientific challenges remain to be further elucidated: (1) what are the structural features and conformational changes of hENT1 during the endogenous adenosine substrate transport? (2) AdoRIs increase extracellular concentration of adenosine by inhibiting hENT1's function, but the exact action mechanism and dynamic details are unclear.

Dilazep, a non-nucleoside AdoRI commonly used in clinic, was selected as the research object to explore the detailed mechanism of inhibiting hENT1. Then, comparative long-time unbiased molecular dynamics (MD) simulations were performed for the three hENT1 systems embedded in the lipid bilayer (*i.e.*, hENT1 complexes with dilazep and adenosine, ligand-free hENT1). Principal component analysis (PCA), free energy landscape (FEL), cluster and channel analyses were combined to investigate slow functional motions and conformational changes in the three hENT1 systems. The key residues of protein-ligand recognition were mined with molecular mechanics/generalized born surface area (MM-GBSA) method; the averaged independent gradient model (aiGM) was also used to graphically investigate their dynamic weak interactions. Several representative conformations of hENT1 during adenosine transport have been observed through the exhaustive analyses of global motion, channel features and molecular recognition, and the possible inhibition mechanism of dilazep has been proposed. The nucleoside transport and dilazep inhibition results in this paper not only contribute to an in-depth understanding of hENT1 working mechanism, but also

provide theoretical guidance for the design of novel non-nucleoside AdoRIs based on receptor structure.

2. Materials and methods

2.1. Preparation of simulation systems

The crystal structure of human equilibrative nucleoside transporter 1 (hENT1) complexed with dilazep was obtained from the Protein Data Bank with entrance code 6OB7 (Wright and Lee, 2019). Then, three site-directed mutations (*i.e.*, L168F, P175A and N288K) for enhancing biochemical stability were recovered to prepare the wild-type hENT1. The missing extracellular and cytosolic loops both were completed by homology modeling package SWISS-MODEL (Waterhouse et al., 2018). Subsequently, the hENT1 structure at apo state can be obtained by removing the ligand molecule (*i.e.*, dilazep). In order to acquire a reasonable hENT1 model in complex with adenosine, an adenosine molecule was bound into the transporter's orthosteric site by molecular docking. The above three systems are referred to as hENT1_{apo}, hENT1_{adenosine} and hENT1_{dilazep}, respectively. The pK_a values of ionizable groups in macromolecules were calculated by H++ (Anandakrishnan et al., 2012), and the missing hydrogen atoms were added with reference to environment pH value of 7.4.

2.2. Molecular docking

Molecular structure of adenosine was constructed using ChemBio3D Ultra 12.0 (Cambridge Soft, Cambridge, MA, USA), and was structurally optimized under the B3LYP-D3/6-311G (d, p) calculation level integrated into Gaussian 09 software (Frisch et al., 2013; Mayo et al., 1990; Grimme et al., 2010; McLean and Chandler, 1980). Molecular docking was carried out with AutoDock vina 1.2.2 package, where Lamarckian genetic algorithm (LGA) sampling was adopted, and a semiempirical potential function was used to rank the intermolecular energy scores between the receptor and ligand (Trott and Olson, 2010). The receptor was programmed to remain rigid while the ligand was considered flexible allowing the single bond to rotate. According to the coordinates of adenosine analog NBMPR in the crystal structure (PDB code: 6OB6 (Wright and Lee, 2019)), the rectangular box center was determined with size of $20 \text{ \AA} \times 20 \text{ \AA} \times 20 \text{ \AA}$ and grid space of 0.375 \AA . The conformation with the lowest energy in the largest cluster was defined as the near native structure, and used for the subsequent MD simulations.

2.3. Molecular dynamics simulation

To explore the mechanism of hENT1-mediated adenosine transport and its inhibition by dilazep, three comparative unbiased molecular dynamics (MD) simulations at 300 K were performed for hENT1_{apo}, hENT1_{adenosine} and hENT1_{dilazep} with Amber 20 package (Case et al., 2020). The above three systems were respectively embedded in the explicit lipid bilayer environment (box size: $101 \text{ \AA} \times 102 \text{ \AA} \times 128 \text{ \AA}$) with a ratio of 3:1 between 1-palmitoyl-2-oleoyl-*sn*-glycero-3-phosphoethanolamine (POPE) and 1-palmitoyl-2-oleoyl-*sn*-glycero-3-phospho-(1'-*rac*-glycerol) (POPG) (Jo et al., 2009) (see Fig. 1A). Parametrization of adenosine, including atomic RESP charges, was obtained using Antechamber module of Amber 20 package (Bayly et al., 1993). Here, Amber ff14SB, GAFF2 and LIPID17 force fields were respectively applied to hENT1 protein, ligands (*i.e.*, adenosine and dilazep) and membrane (*i.e.*, POPE/POPG bilayer) (Maier et al., 2015; Wang et al., 2004; Dickson et al., 2014). TIP3P water and 0.15 M NaCl both were added to solvate and neutralize the membrane protein systems with Joung/Cheatham ion parameters (Jorgensen et al., 1983). The solvated systems totally contained $\sim 120,000$ atoms and the simulation details were mentioned in Table S1.

Before MD simulations, a three-step energy optimization was carried out as follows: (1) all solutes were constrained with the force constant of

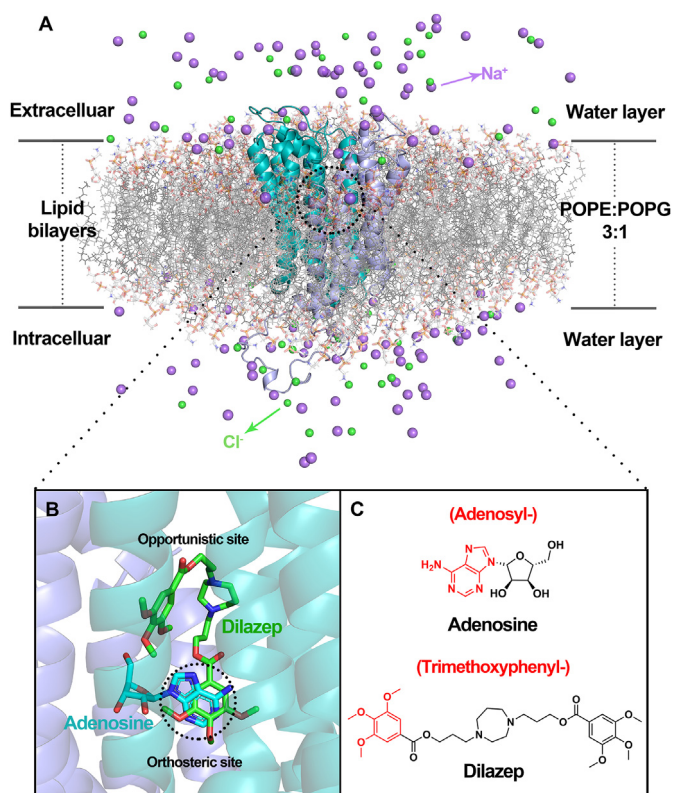


Fig. 1. (A) Overview of hENT1 embedded in the lipid bilayer. The hENT1 protein is shown in cartoon representation. POPE and POPG are shown in lines, and counter ions are illustrated by spheres (purple for Na^+ and blue for Cl^-). Water molecules are not displayed for clarity. (B) The postures of adenosine and dilazep in binding cavity are shown in sticks (blue for adenosine and green for dilazep). (C) Molecular structures of adenosine and dilazep. The overlapping moieties in the orthosteric site are marked in red. (For interpretation of the references to color in this figure legend, the reader is referred to the Web version of this article.)

$100 \text{ kcal mol}^{-1} \cdot \text{\AA}^{-2}$, containing 20000 steps of steepest descent and 20000 steps of conjugate gradient minimization; (2) the solute-membrane system was optimized based on the same force constant and steps; (3) after removing all geometry constraints, the same minimization steps were followed to optimize the structure of the protein-membrane-water system. The convergence criterion of three minimizations is energy difference of neighboring conformations less than $1.0 \times 10^{-4} \text{ kcal mol}^{-1} \cdot \text{\AA}^{-1}$.

After energy minimization, the system was then slowly heated to 300 K through two sequential processes, during which all solutes are fixed with the force constant of $10 \text{ kcal mol}^{-1} \cdot \text{\AA}^{-2}$. Specifically, the system was heated to 100 K in 5 ns using Langevin thermostat (Izaguirre et al., 2001); subsequently, the production temperature was raised to 300 K in 5 ns, and the anisotropic Berendsen weak-coupling barostat was used to regulate the pressure simultaneously (Berendsen et al., 1984). In order to reduce atomic crash, 50 ns ($5 \text{ ns} \times 10 \text{ times}$) equilibration was performed under the NPT ensemble; next, three non-restraint MD simulations at 300 K were performed for 1 μs adopting SHAKE algorithm to constrain the hydrogen-containing atoms (Ryckaert et al., 1977). The particle mesh Ewald (PME) method was employed to evaluate the electrostatic interactions with cut-off of 16 \AA , and van der Waals interactions were computed with cut-off of 16 \AA (Essmann et al., 1995). The integration step was set as 2 fs, and the conformational snapshots were collected every 20 ps, so total 50,000 conformations were obtained during each productive MD simulation. The simulated trajectories were monitored by VMD 1.9.4, and the conformational analyses were performed using CPPTRAJ module embedded in Amber 20 package (Humphrey et al., 1996; Roe and Cheatham, 2013).

2.4. Principal component analysis

Principal component analysis (PCA) is a standard method for finding global, correlated motions from MD trajectories through dimensionality reduction. PCA has been successfully applied to some functional motion studies in many biological systems (Wu et al., 2020, 2022). The PCA is mainly based on the construction and diagonalization of the covariance matrix, whose element C_{ij} is given by:

$$C_{ij} = \langle (x_i - \langle x_i \rangle)(x_j - \langle x_j \rangle) \rangle$$

where x_i / x_j is the coordinate of the i th/ j th atom of the systems, and $\langle \dots \rangle$ denotes an ensemble average. The matrix is diagonalized to get a set of eigenvectors (i.e., principal components) and eigenvalues, which determine the directions and magnitudes of the corresponding motions. Principal components (PCs) are sorted in terms of the eigenvalue contribution to the whole motion. In generally, the large-scale motions are often related to biological function; while for other PCs with lower eigenvalues, the corresponding motions are composed of high-frequency local vibrations. To get the functional motions from a MD simulation, the entire MD trajectory must be projected along the directions described by the first few selected eigenvectors to filter out non-functional motions. Through superimposing the two extreme projection structures to the initial one, the detailed functional motion information can be distinctly revealed with the porcupine map, where the length and orientation of cone in each C_{α} atom respectively represent motion magnitude and direction. In this work, PCA was performed for the C_{α} atoms in hENT1_apo, hENT1_adenosine and hENT1_dilazep based on their MD trajectories.

2.5. Free energy landscape

Free energy landscape (FEL) is mainly used to investigate molecular motions and conformational changes for biological systems. Free energy basins determine the population and stability of functionally distinct states, while the inter-basin barriers correspond to the transient states connecting them. The first (PC1) and second principal component (PC2) both serve as reaction coordinates for the mapping of free energy surface diagram (Maisuradze et al., 2010). The relative free energy between two states is defined as follows:

$$\Delta G_{(PC1, PC2)} = -k_B T \ln P_{(PC1, PC2)}$$

where k_B is the Boltzmann constant, T expresses the absolute temperature in Kelvin and $P_{(PC1, PC2)}$ is the probability distribution of systems along with the PC.

2.6. Cross-correlation analysis

The internal motion modes of proteins play a significant role in allosteric processes. The dynamical cross-correlation map (DCCM) is an efficient way for determining the internal dynamics of proteins. DCCM can effectively reveal the detailed movements of a residue relative to another residue in proteins. The cross correlation coefficient C_{ij} between C_{α} atoms of residues i and j is estimated based on an ensemble average extracted from MD trajectories (Ichiye and Karplus, 1991):

$$C_{ij} = \frac{\langle \Delta r_i \cdot \Delta r_j \rangle}{(\langle \Delta r_i^2 \rangle \langle \Delta r_j^2 \rangle)^{1/2}}$$

where $\Delta r_i / \Delta r_j$ represents the displacement of the i th/ j th C_{α} atom relative to its average position. In this work, C_{ij} fluctuates from -1 to 1 , among which a positive C_{ij} value characterizes the positively correlated motion between residues i and j , while a negative value represents the opposite motion of residue i relative to j . To visually observe motion

modes, color-coded modes were utilized to display the extent of correlated movements between residues.

2.7. Prediction of binding free energies

Binding affinity of the three complexes (*i.e.*, hENT1_apo, hENT1_adenosine and hENT1_dilazep) was evaluated using MM-GBSA method (Sun et al., 2014a, 2014b). The conformations were extracted from their MD trajectories every 5 ns intervals from the last 200 ns simulations. Based on the total 40 snapshots, the average binding free energy was calculated using the following equation:

$$\Delta G_{bind} = \Delta H - T\Delta S = (\Delta E_{VDW} + \Delta E_{ELE} + \Delta G_{GB} + \Delta G_{GBSUR}) - T\Delta S$$

where ΔH represents the total enthalpy change and T is absolute temperature in Kelvin. ΔS refers to the total entropy change calculated using normal mode method (Genheden et al., 2012); ΔE_{VDW} refers to the non-polar fraction of intramolecular energy under vacuum, while ΔE_{ELE} indicates the electrostatic section. ΔG_{GB} and ΔG_{GBSUR} correspond to the hydrophilic and hydrophobic parts of solvation free energy, respectively. The former is computed using GB model developed by Onufriev et al. (2004) and the latter is solved using the following empirical equation:

$$\Delta G_{GBSUR} = \gamma \times \Delta SASA + \beta$$

where γ and $\Delta SASA$ characterize surface tension and difference in solvent-accessible surface areas (SASA), respectively. In this work, the empirical parameters γ and β were $0.005 \text{ kcal mol}^{-1} \cdot \text{\AA}^{-2}$ and 0 kcal mol^{-1} , respectively. The solvent and solute dielectric constants were set to 80 and 1, respectively.

2.8. Weak interaction analysis

The interactions in biochemical systems are mainly divided into bonded and nonbonded interactions. Bonded interactions consist of covalent and ionic bonds, which are defined as having relatively high bond strength. Nonbonded interactions are generally an order of magnitude weaker and are often referred to as weak interaction, mainly involving hydrogen bonds, halogen bonds, pi-pi stack, van der Waals forces and steric hindrance, etc. The weak interaction from single frame cannot fully reflect dynamic information between protein-ligand, but the average value calculated from continuous trajectory of MD simulation can offer more intuitive and smooth isosurfaces. In this work, the protein-ligand complex (*i.e.*, hENT1_adenosine and hENT1_dilazep) after 1 μs MD simulation was set as the initial structure; an extra 1 ns MD simulation was performed with fixed ligand, and total 1000 conformations were collected for subsequent calculation of ensemble averaging.

Averaged independent gradient model (aIGM) was adopted for studying the average weak interaction between protein-ligand, which has been embedded in Multiwfn package (Lu and Chen, 2012). In aIGM, a real space function δg_{avg}^{inter} was defined. The average interaction between a set of self-defined fragments $\{A\}$ can be calculated with the following equation (Lefebvre et al., 2017):

$$\delta g_{avg}^{inter}(r) = g_{avg}^{IGM, inter}(r) - g_{avg}^{inter}(r) = \left| \sum_A \text{abs} \left(\sum_{i \in A} \nabla \rho_i(r) \right) \right| - \left| \sum_A \left(\sum_{i \in A} \nabla \rho_i(r) \right) \right|$$

where i is atomic index, ρ_i is the built-in spherically symmetrized electron density of atom i at its isolated state, and the $\langle \dots \rangle$ symbol stands for an ensemble average. ρ and λ_2 refer to promolecular electron density and the second largest eigenvalue of Hessian matrix, respectively. The result of aIGM analysis was plotted with $\delta g_{avg}^{inter}(r)$ isosurface map colored by averaged $\text{sign}(\lambda_2)\rho$.

3. Results and discussion

3.1. Structures of hENT1 systems

Fig. 1 shows the overall architecture and substrate binding site of the hENT1 system. hENT1 contains eleven transmembrane helices (TMs), which can be divided into two major domains referred to as the N-terminal domain (NTD, TM1-6) and C-terminal domain (CTD, TM7-11). The NTD and CTD are almost symmetrical (see Fig. 1A), similar to the major facilitator superfamily (MFS) (Quistgaard et al., 2016). Two large disordered loops are located between TM1-2 and TM6-7, denoted as extracellular loop and cytosolic loop, respectively. The initial structures of hENT1_apo, hENT1_adenosine and hENT1_dilazep are all in an outward-facing state.

In order to verify the rationality of molecular docking, the predicted model of hENT1_adenosine and the crystal structure of hENT1_NBMMPR were superimposed together (see Fig. S2A). It could be seen that adenosine almost completely overlaps with the adenosyl moiety of NBMMPR, indicating this docking strategy is reliable. The detailed interaction mode of adenosine was shown in Fig. S2B. Three polar residues D341, R345 and N407 are involved in ribose recognition. Comparing the binding posture of adenosine with that of dilazep, it is found that one of trimethoxyphenyl rings in dilazep serves as adenosyl moiety in the endogenous adenosine substrate to competitively occupy the orthosteric site of hENT1. In addition, the other trimethoxyphenyl ring occupies the opportunistic site near the extracellular side, which may be the crucial factor for its significant inhibitory activity against hENT1 (see Fig. 1B and C).

3.2. Overall structural convergence

Three comparative unbiased 1 μs MD simulations were carried out for hENT1_apo, hENT1_adenosine and hENT1_dilazep. The stability of simulation process was firstly monitored by potential energy analysis. Although potential energy only acts as an assistant factor in determining the convergence of simulation, all three systems achieve energy equilibrium in the production MD simulations with low fluctuations (see Fig. 2E). Fig. 2A and B shows root mean square deviation values (RMSDs) of C_α atoms relative to the initial structure, as well as their probability distributions. The sudden increase in RMSD around 0.7 μs is caused by a combination of local folding of the extracellular loop and disordered swing of the cytosolic loop (the hENT1_apo system, see below). The last 0.8 μs MD trajectories of the three systems keep comparatively stable, and are used for subsequent flexibility and conformation analyses. As shown in Fig. 2A and B, the average RMSD value of hENT1_adenosine is obviously greater than hENT1_apo and hENT1_dilazep, which indicates that the binding of adenosine increases the flexibility of the whole system. While after binding dilazep, the average RMSD value of hENT1_dilazep declines to about 5 \AA , indicating that the inhibitor significantly constraints the overall motion of hENT1 and leads to a static non-functional state. To sum up, the rank of molecular flexibility for the above three systems is: hENT1_adenosine ($\sim 8.1 \text{ \AA}$) > hENT1_apo ($\sim 6.7 \text{ \AA}$) > hENT1_dilazep ($\sim 5.0 \text{ \AA}$).

As an important complement to the global motion convergence, Fig. 2C shows the variation of the gyration radius versus simulation time in the three systems. At the beginning of MD simulations, the upward trend of gyration radius is related to solvent effect, being extended under solution condition. Subsequently, with the formation of thermodynamically stable conformation, the investigated systems gradually shrink. The significant rise in radius of gyration around 0.4 μs corresponds to the opening movement of the extracellular loop (the hENT1_apo system, see below). Interestingly, the rank of gyration radius is exactly opposite to that of RMSD in the three investigated systems (*i.e.*, hENT1_dilazep > hENT1_apo > hENT1_adenosine). With reference to the current working model of MFS transporters (Deng et al., 2015; Nomura et al., 2015; Qureshi et al., 2020), it can be inferred that the structural contraction in hENT1_adenosine may be closely related to functional conformational transitions.

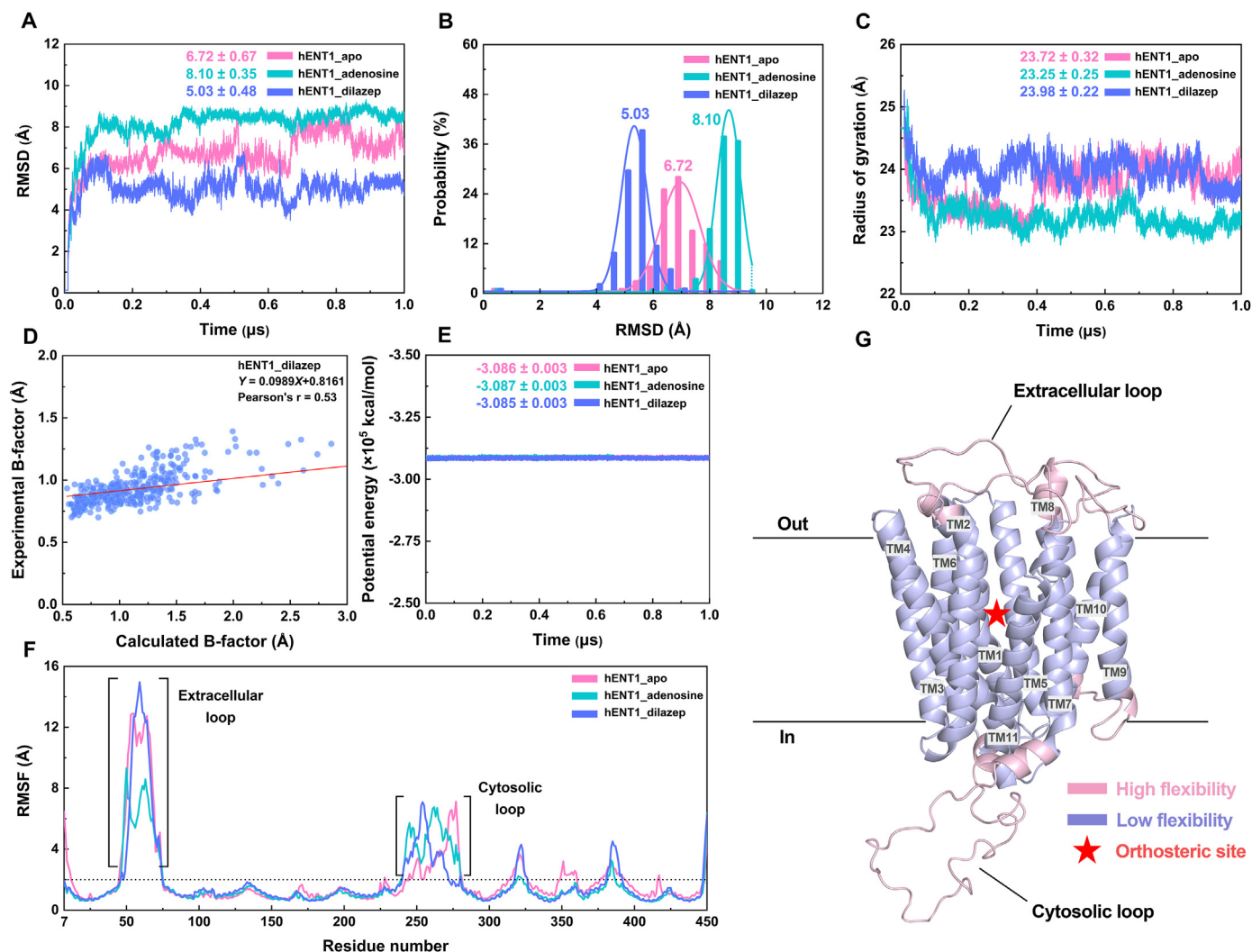


Fig. 2. Comparative MD analyses of the hENT1_apo, hENT1_adenosine and hENT1_dilazep systems. (A) RMSD values of all the C α atoms. (B) The probability distribution of RMSDs. (C) Radius of gyration over simulation time. (D) The correlation of calculated B-factors with experimental data. (E) Potential energy over simulation time. (F) RMSF values of all the C α atoms. (G) The flexibility distribution of hENT1. Pink and blue colors represent high and low flexibility regions, respectively. (For interpretation of the references to color in this figure legend, the reader is referred to the Web version of this article.)

To further investigate protein flexibility at residue level, the root mean square fluctuation values (RMSFs) were compared for the three hENT1 systems. There is high correlation between experimental and calculated B-factors with a positive correlation coefficient of 0.53, and the reliability of MD trajectories is proven again (see Fig. 2D). As shown in Fig. 2F, the RMSF distributions at TMs appear to be similar with low fluctuations in the three systems. High RMSF regions are basically located in the extracellular loop, cytosolic loop and the connection areas between different TMs (see Fig. 2G). Among them, the extracellular loop is characterized with the largest RMSF value and its flexible rank is consistent with that of gyration radius (*i.e.*, hENT1_dilazep > hENT1_apo > hENT1_adenosine). It means the large-scale flexible movement of the extracellular loop may be directly involved in the functional structural contraction of hENT1. Previous studies have suggested that the extracellular loop contains N-linked glycosylation sites and is involved in membrane trafficking and protein folding (Sundaram et al., 2001; Bicket and Coe, 2016). Here, simulation data suggests that the extracellular loop may play an important role in the functional structural contraction of hENT1 and will be further clarified in the following analyses.

To further explore the structural contraction in hENT1_adenosine, residue contact map was used to describe the motion status of the three hENT1 systems. If the distance between two residues in a biomacromolecular system is less than 4.5 Å, they are considered to have a

contact. Fig. 3 shows the differences of contact residues between the initial (at 0 μ s) and the final (at 1 μ s) snapshots in hENT1_apo, hENT1_adenosine and hENT1_dilazep. In the above three systems, the numbers of contact residues in initial structures are 524/544/567, increasing to 544/604/586 in each final structure. Common contact residues are 363/399/397, while the specific contact residues are 161/181, 145/205 and 170/189, respectively. In this work, two parameters (*i.e.*, contact similarity and reduction rate) are defined to characterize the conservativeness of contact residues, as well as the contraction degree of the systems. The contact similarity is calculated by common contacts divided by all contacts that contain common and specific contact in initial and final structures. The reduction rate is calculated with the difference value between the number of specific contacts in the two structures divided by the total number of contacts in the initial structure. As a highly flexible protein, the contact similarity of hENT1_apo, hENT1_adenosine and hENT1_dilazep is relatively low and close to each other (51.49%/53.27%/52.51%), showing that the inherent contact network is prone to rearrangement. Compared with hENT1_apo and hENT1_dilazep (-3.82%/-3.35%), hENT1_adenosine possesses an obviously higher reduction rate (-11.03%). It is consistent with the previous analysis of gyration radius, together demonstrating that hENT1_adenosine undergoes a function-related contractive movement.

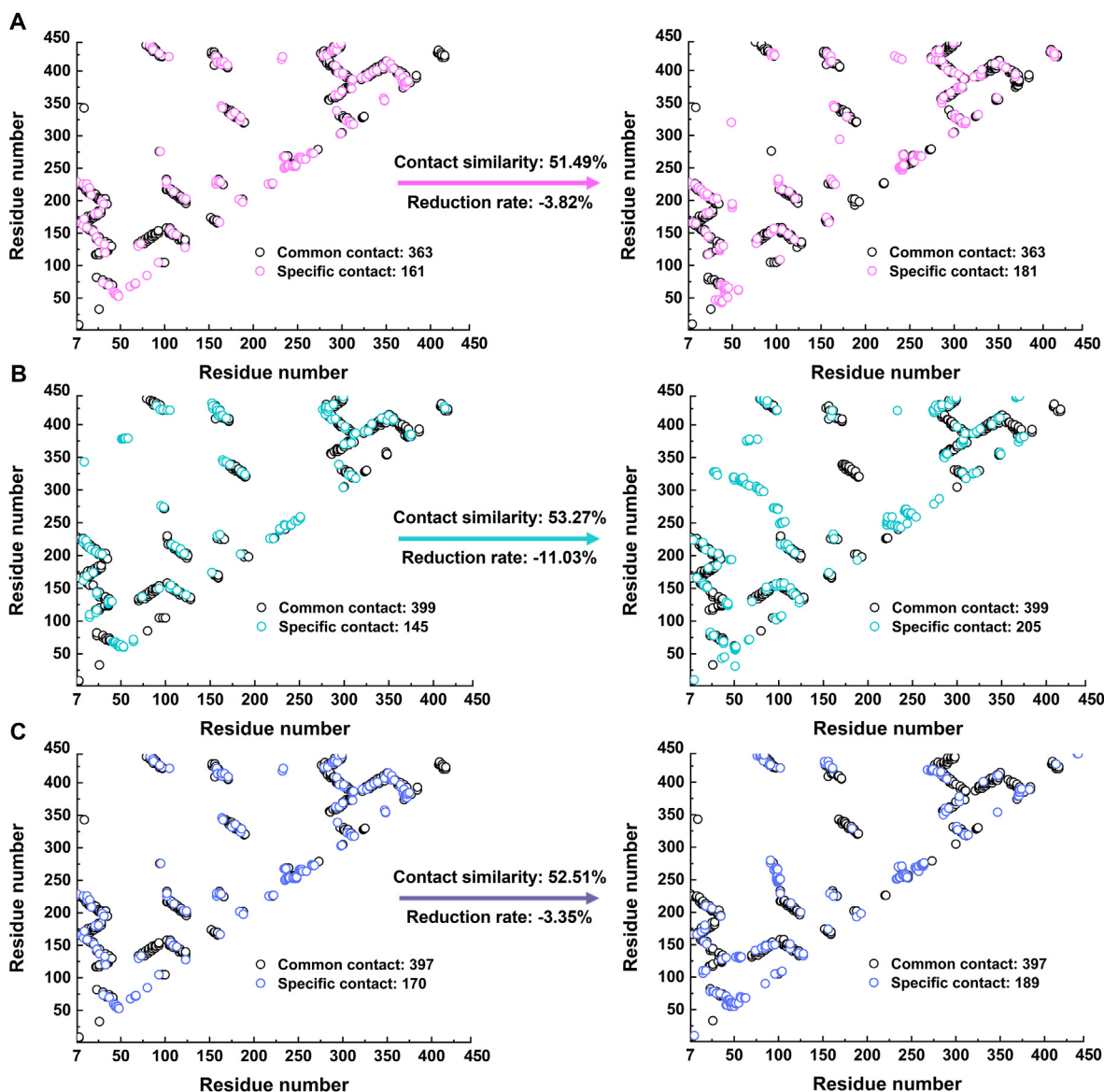


Fig. 3. Residue contacts maps of the hENT1_apo (A, in pink), hENT1_adenosine (B, in green) and hENT1_dilazep systems (C, in blue). The left side represents the initial structures, and the right side represents the last frames of the simulation. (For interpretation of the references to color in this figure legend, the reader is referred to the Web version of this article.)

3.3. Functional conformational changes

As mentioned above, the consistent rank of gyration radius with extracellular loop flexibility in the three hENT1 systems (*i.e.*, hENT1_dilazep > hENT1_apo > hENT1_adenosine) implies that the large-scale flexible movement of extracellular loop may have a correlation with functional structural contraction of the protein. Then, PCA was performed to further discuss the impact of ligands on the motion mode and conformational change of hENT1. The top principal components (PCs) usually contain the most critical conformational information, and can reveal its functional movements. Fig. S3 shows the distributions of the top 50 eigenvalues for hENT1_apo, hENT1_adenosine and hENT1_dilazep. With the increment of PC index in each system, the proportion of eigenvalues rapidly decreases towards zero. In the hENT1_apo, hENT1_adenosine and hENT1_dilazep systems, the first two PCs together cover approximately 62.09%/60.93%/64.21% of the conformational information.

To further investigate the conformational distributions along PC1 and PC2, Fig. 4A–C shows free energy landscapes (FEL) in the hENT1_apo,

hENT1_adenosine and hENT1_dilazep systems, respectively, with deeper color indicating lower free energy. The FEL of hENT1_apo and hENT1_dilazep are more divergent, with six and four energy basins, respectively (see Fig. 4A and C). However, hENT1_adenosine has three adjacent low free energy regions, and is more compact in conformational space (see Fig. 4B). As shown in Fig. 4D–F, the domains with obvious conformational differences are mainly located in the extracellular loop, as well as the cytosolic loop. In detail, the cytosolic loop folds up and contacts with the intracellular side of membrane. The different conformational changes of the extracellular loop in the three systems seem to represent a meaningful substrate-regulated gating strategy of the central cavity. In apo state, the extracellular loop has an obvious open-close movement (see Fig. 4D and Fig. S4). After the association with adenosine, the extracellular loop inclines to be closed conformations which already exist in apo state (*i.e.*, M1 and M4), and further shrinks to prevent substrate dissociation (see Fig. 4E and Fig. S4). hENT1 has been shown to mediate low-affinity transport of nucleobases (Ward et al., 2000; Yao et al., 2011), but previous studies also indicated that the absence of extracellular loop does not affect general functional properties of transport and inhibition

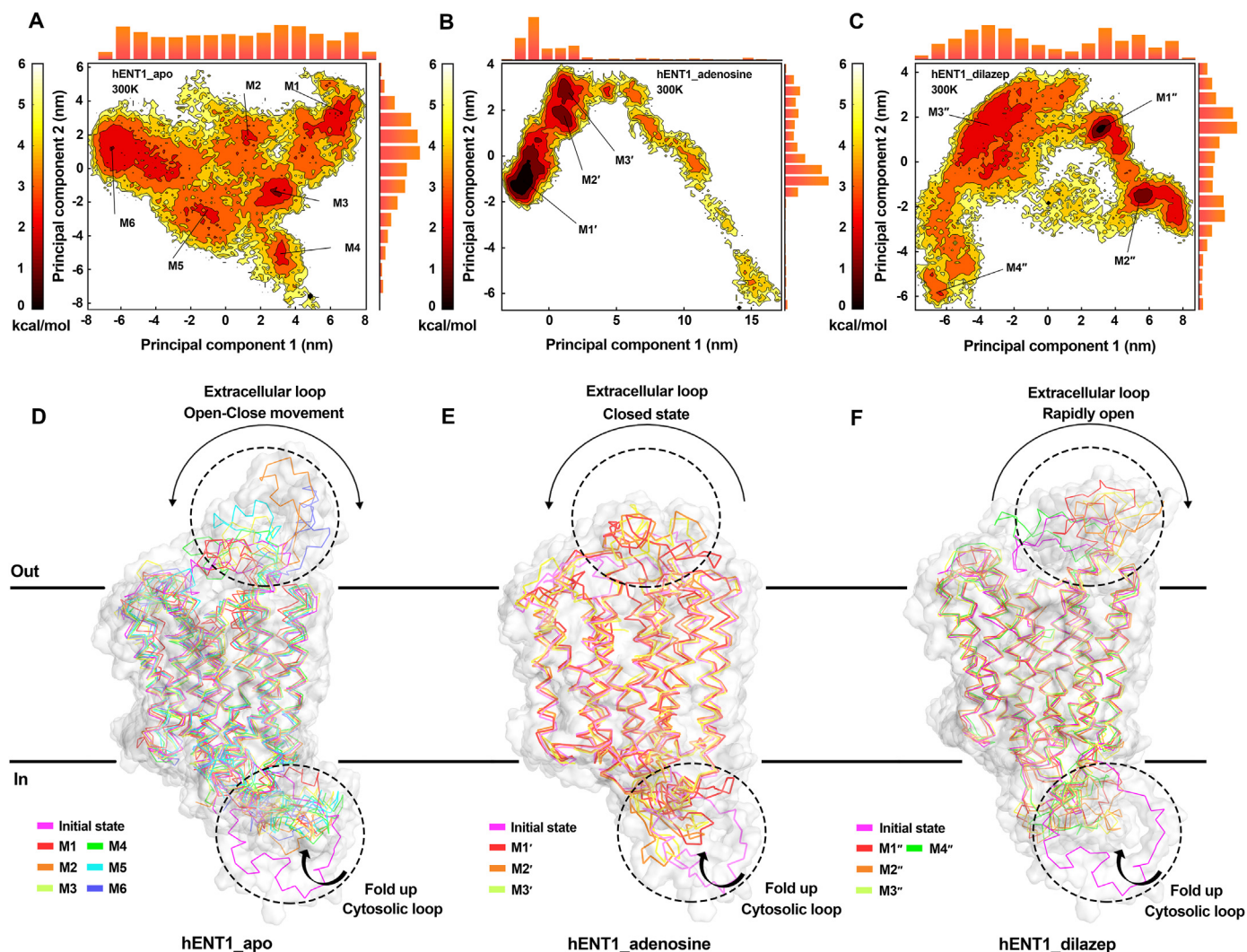


Fig. 4. Free energy landscapes versus the first two PCs and representative conformations in the hENT1_apo (A, D), hENT1_adenosine (B, E) and hENT1_dilazep systems (C, F). The protein is depicted in surface and ribbon models.

(Aseervatham et al., 2015). Therefore, the observed functional closed movement of extracellular loop seems to be an extra auxiliary insurance to ensure that the endogenous adenosine is firmly locked in the transport cavity. It is worth mentioning that such substrate-regulated loop gating strategy is ubiquitous in many proteins, like β -lactamase NDM-1 (Zhang and Hao, 2011). On the contrary, when binding to dilazep, the extracellular loop remains open (*i.e.*, M1''-M4'') rather than closed conformations, which also exist in hENT1_apo (*i.e.*, M2, M5 and M6). It can be inferred that the rapid opening of the extracellular loop provides a dissociation channel for dilazep, reflecting the specific repelling of hENT1 to exogenous substrates, which may be one of the evolution self-rescue pathways during the process of inhibition (see Fig. 4F and Fig. S4).

To further clarify motion magnitudes and directions of the most critical conformational changes, the 1st and 2nd slowest motion modes of the three systems were described with cone model. As shown in Fig. 5, the major conformational changes occur in the extracellular side of eleven TMs. By observing the 1st and 2nd slowest motion modes of hENT1_apo (see Fig. 5A and D), the motion magnitudes of TMs are relatively small except for TM8, whose motion direction is towards the inner side of hENT1. Compared with hENT1_apo, the motive magnitudes of the two slowest motions in hENT1_adenosine are dramatically enhanced (see Fig. 5B and E). For example, the functional movements of TM1, TM2, TM4 and TM8 are relatively obvious and point to central axis,

representing a large-scale inward contractive tendency near the extracellular side. It is in line with the above analyses of gyration radius and residue contacts. The inward contractive motion model of TMs fits well with the current working mechanism of MFS transporters, namely rocker-switch model (Drew and Boudker, 2016). There are an obvious inter-domain motion in the two symmetric bundles (*i.e.*, NTD and CTD) during the transition between gate-formation and gate-disruption steps, allowing the substrate to alternate into either side of the membrane (Mitchell, 1957). Therefore, the inward structural contraction of hENT1_adenosine can be corresponded to the conformational transitions from the outward-facing to occluded state in rocker-switch model. In addition, the magnitudes of the 1st and 2nd slowest motion modes in hENT1_dilazep are greatly suppressed relative to hENT1_adenosine (see Fig. 5C and F). The inhibitor dilazep hinders the inward contractive movement of TMs and breaks the functional conformational transitions of hENT1, which is consistent with the currently inferred inhibitory mechanism (Wright and Lee, 2019).

3.4. Internal dynamics of hENT1

Insights into the internal dynamics of hENT1 induced by ligand binding help to reveal the inhibitory effect by dilazep. To comprehensively explore the internal dynamic-dependent differences of hENT1 binding with different ligands, the dynamical cross-correlation map

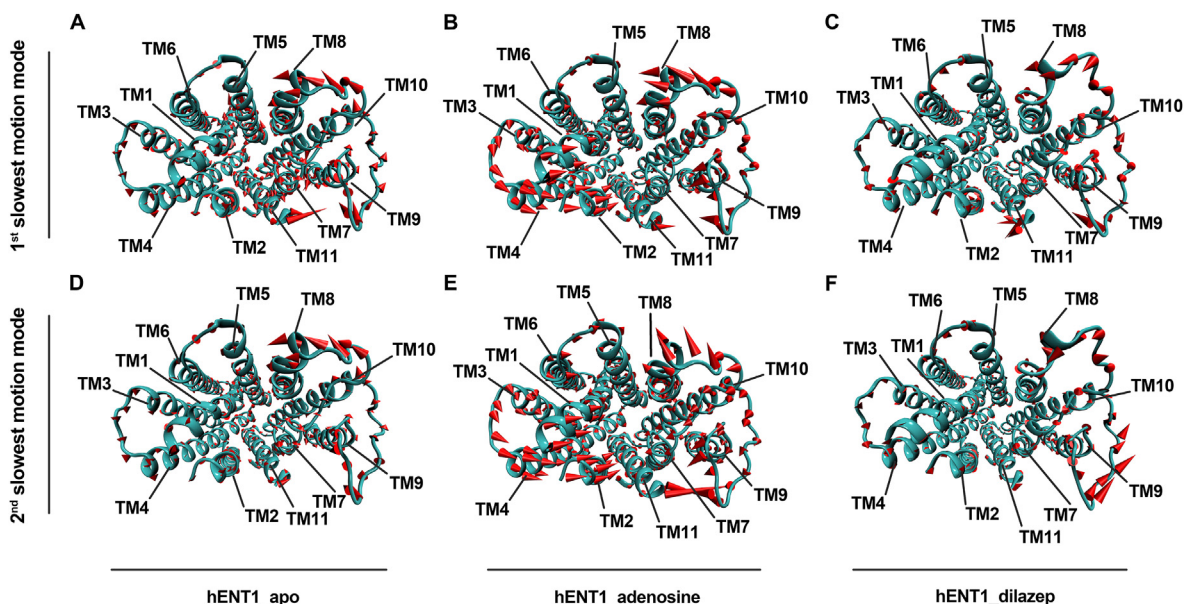


Fig. 5. The 1st and 2nd slowest motion modes in the hENT1_apo (A, D), hENT1_adenosine (B, E) and hENT1_dilazep systems (C, F). For clarity, the extracellular and cytosolic loops are not displayed.

(DCCM) analysis was performed based on the MD trajectories of hENT1_apo, hENT1_adenosine and hENT1_dilazep, respectively (see Fig. 6). The correlated motion of a certain region relative to itself is characterized by the diagonal, while the off-diagonal regions represent the relative movement between different residues.

As shown in Fig. 6, ligand binding has a notable impact on the structural dynamics of hENT1. All three systems have two distinct motion correlation regions (*i.e.*, NTD and CTD), showing clear inner motion positive correlation. In addition, there is obvious negative motion correlation between the extracellular loop and all TMs (*i.e.*, R1-R7), which refers to the open-close movements of the extracellular loop. Compared with hENT1_apo and hENT1_adenosine (see Fig. 6A and B), the negative correlation motions in the R1 to R4 regions of hENT1_dilazep were significantly increased. The stronger inverse-synergistic movement revealed that dilazep can induce a large and rapid opening of the extracellular loop (see Fig. 6C). The presence of adenosine strengthens the positive correlated motions in the region R8 relative to hENT1_apo, which is related to the synergistic movements between NTD and CTD (see Fig. 6B); while the binding of dilazep not only greatly enhances the negative correlation motions in the region R8 to break the inherent

synergistic effects, but also extremely boosts the inner positive correlation motions of NTD (see Fig. 6C).

In conclusion, the binding of different ligands can significantly change the internal dynamic behavior of hENT1. Dilazep can disrupt the normal synergistic movements between NTD and CTD.

3.5. Conformational transitions in the transport cycle of hENT1

The analytical results of gyration radius, residue contacts and slow motion modes together indicate that the hENT1_adenosine system undergoes a functional contraction during the MD simulation, which is closely related to its conformational transitions from the outward-facing to occluded state. The inhibitor dilazep hinders the inward contractive movements of TMs to break the normal nucleoside transport function of hENT1. To reveal the details of adenosine transport and the exact inhibitory mechanism of the non-nucleoside AdoRi dilazep, it is necessary to capture the representative conformations in the transport cycle of hENT1. In the two available inhibitor-bound crystal structures (*i.e.*, hENT1 in complex with dilazep and NBMPr), the narrowest constriction point at the extracellular side occurs between M33 of TM1 and P308 of

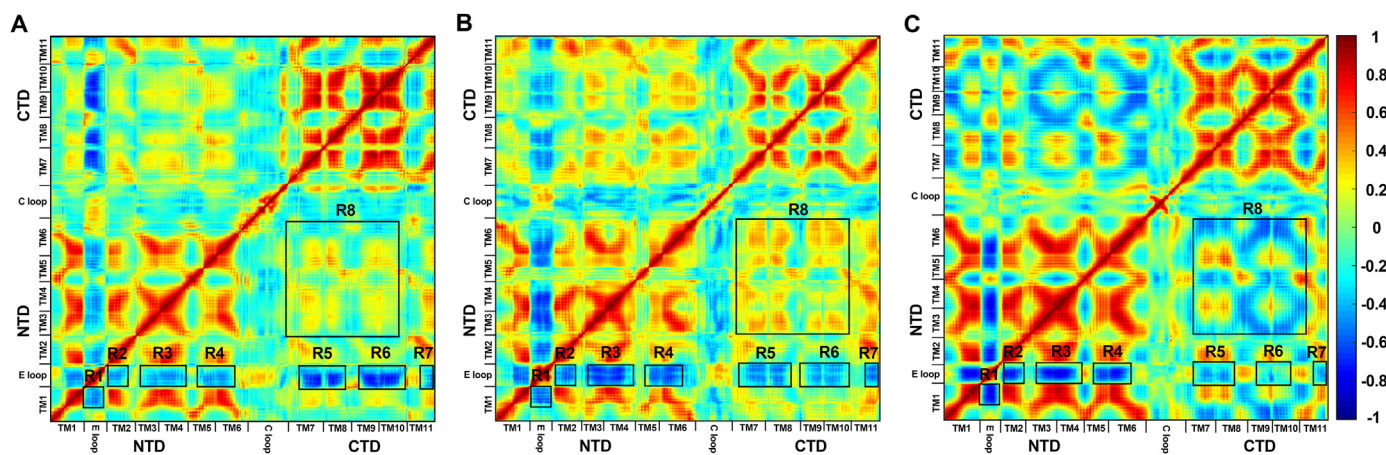


Fig. 6. Dynamical cross-correlation maps of C_{α} atoms for the hENT1_apo (A), hENT1_adenosine (B) and hENT1_dilazep systems (C). The color-coded modes were used to visualize the different correlated motion patterns. Strongly positive correlated and negative correlated motions are colored in red and blue, respectively. (For interpretation of the references to color in this figure legend, the reader is referred to the Web version of this article.)

TM7, and this region was named the extracellular thin gate. Meanwhile, some hydrophobic residues of TM4, TM5, TM10 and TM11 form the intracellular thick gate, occluding access from the cytosolic side. Notably, in the crystal structure of hENT1 in complex with NBMMPR, the thin gate blocks NBMMPR from releasing into the extracellular side freely, representing the only outward occluded conformation captured experimentally.

According to the rocker-switch alternating access model of hENT1 transport (Deng et al., 2015; Nomura et al., 2015; Qureshi et al., 2020; Drew and Boudker, 2016; Mitchell, 1957), the extracellular thin gate is occluded first upon substrate binding (i.e., the outward occluded state); then, the extracellular side of hENT1 further shrinks to reach the occluded state; finally, the conformational rearrangement of cytosolic side yields inward-facing states. It means the occlusion of the extracellular thin gate is a prerequisite for the formation of occluded and even inward-facing states. Due to the occluded state is considered to be metastable, this conformation has only been observed in three cases so far (Qureshi et al., 2020; Yin et al., 2006; Fukuda et al., 2015). To capture the key conformers including the outward open, outward occluded and occluded states from 50,000 frames, the full occlusion of the extracellular thin gate was set as a time node to distinguish different functional states in the transport cycle of hENT1. Therefore, the distance between the C_{α} atoms of the narrowest constriction points M33 and P308 in hENT1_apo, hENT1_adenosine and hENT1_dilazep were monitored during the MD simulations to find the time window when the extracellular thin gate is completely occluded.

As shown in Fig. 7A–C, the average distance between the C_{α} atoms of M33 and P308 in the investigated three systems is basically similar; nevertheless, the distance fluctuates greatly in hENT1_apo and hENT1_adenosine, while remains very stable in hENT1_dilazep; more importantly, the distance in the apo and adenosine-bound systems decreases significantly to about 7 Å in a specific period. Fig. 7D and E respectively show the representative structures with the narrowest thin gate in hENT1_apo and hENT1_adenosine, where the extracellular thin

gate is completely occluded, preventing the uptake of nucleoside substrates. In Fig. 7F, dilazep is stuck in the thin gate, contacting tightly with M33 and P308 in the opportunistic site.

Subsequently, the conformational cluster analyses were performed based on the trajectories corresponding to the thin gate occlusion to find the potential metastable occluded state (i.e., 300–400 ns for hENT1_apo and 700–900 ns for hENT1_adenosine). To capture the outward open state, the same cluster analyses were performed based on the remaining equilibrium trajectories of the above two systems (i.e., 400–1000 ns for hENT1_apo and 200–700 ns for hENT1_adenosine). Meanwhile, as a comparison, the whole equilibrium trajectory of hENT1_dilazep was also used for clustering to find possible important conformers (i.e., 200–1000 ns). The cut-off value in the cluster analysis was set to 2 Å to distinguish small differences in conformations. As a result, a large number of clusters are obtained for the long-time trajectories (see Table S2 and Figs. S5–S7).

As depicted in Fig. 8, by examining the representative conformation of each cluster, we captured the outward open and outward occluded states of the hENT1_apo system, as well as the outward occluded and occluded states of the hENT1_adenosine system. The outward occluded state is found in both hENT1_apo and hENT1_adenosine, suggesting that hENT1 possesses the inherent conformational transition ability from the outward open to outward occluded state in the absence of binding ligands. Notably, the metastable occluded state only exists in hENT1_adenosine, which is consistent with the previous studies that the absence of ligand will greatly increase the energy barrier reaching the occluded conformation in the MFS family GLUT transporter (Drew et al., 2021). Due to the limitation of sampling interval, the fully outward open state in hENT1_adenosine was not captured, but an unstable intermediate conformation between the outward open and outward occluded states was found unexpectedly. In this intermediate, the extracellular thin gate is not completely occlude.

Through superimposition of the occluded state in hENT1_adenosine with the outward open state in hENT1_apo, it is found that the transitions

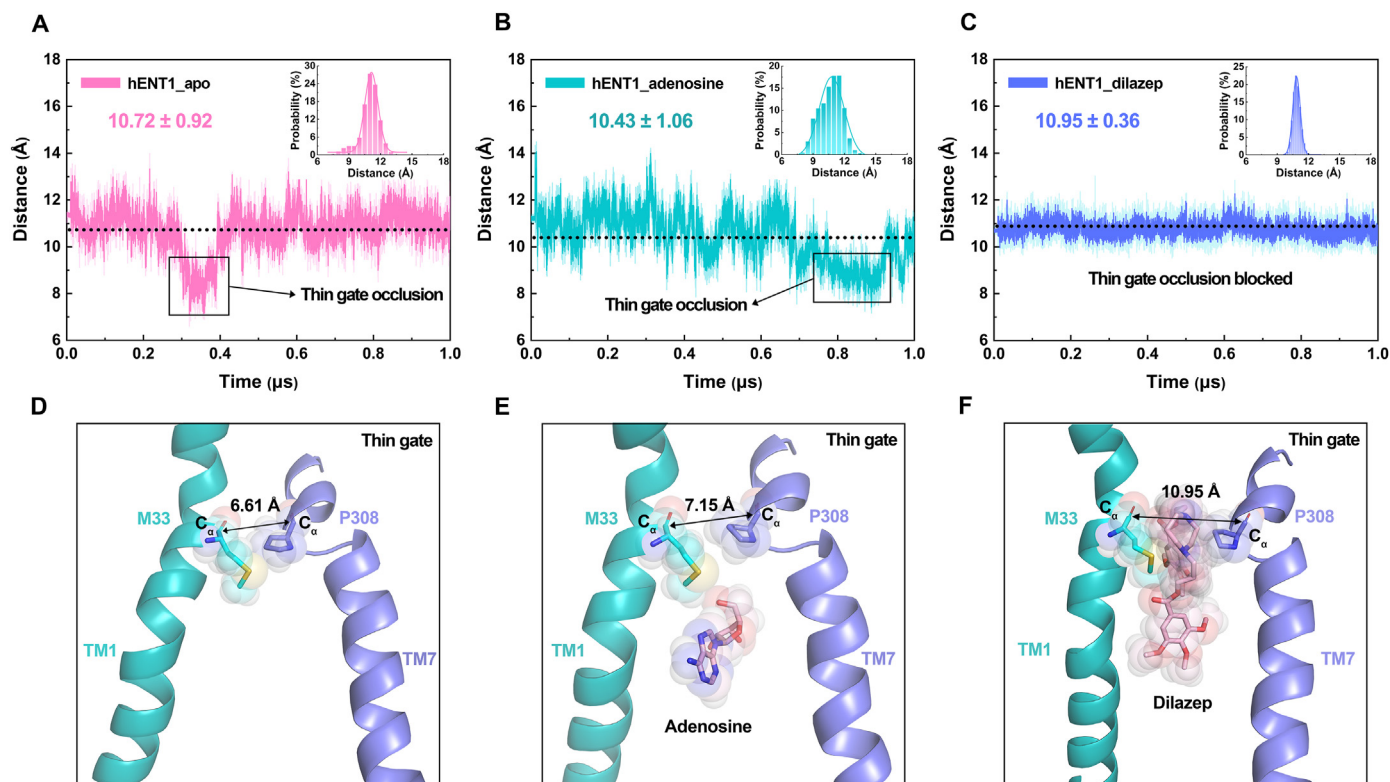


Fig. 7. The distance between the C_{α} atoms of the narrowest constriction point M33 and P308 in the hENT1_apo (A), hENT1_adenosine (B) and hENT1_dilazep (C) systems over simulation time. The representative structures of thin gate occlusion in the hENT1_apo (D) and hENT1_adenosine (E) systems. The representative structure of thin gate occlusion blocked in the hENT1_dilazep system (F). Both sphere and stick models are used to depict M33, P308, adenosine and dilazep.

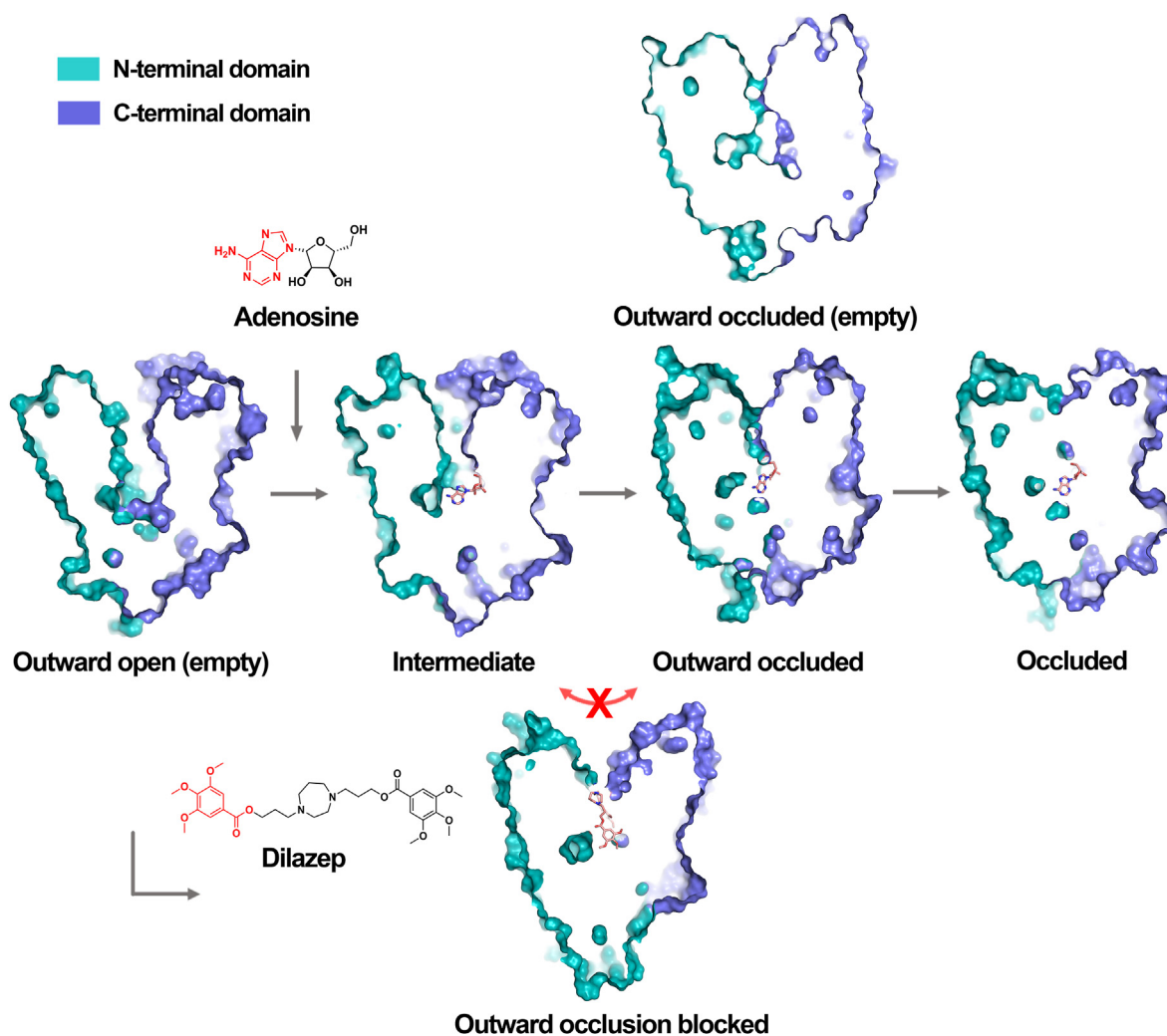


Fig. 8. The functional conformational transitions captured from the MD simulations of the hENT1_{apo}, hENT1_{adenosine} and hENT1_{dilazep} systems. The surface models of NTD and CTD are colored in green and blue, respectively. The extracellular and cytosolic loops are not displayed for clarity. (For interpretation of the references to color in this figure legend, the reader is referred to the Web version of this article.)

from the outward open to occluded state are mainly driven by TM1, TM2, TM7 and TM9 (see Fig. S8). Different from the 6 + 6 topology of MFS transporters (*i.e.*, TM1–12), TM12 is absent in hENT1 and TM9 is arranged to fit into the space occupied by both TM9 and TM12 in MFS (Wright and Lee, 2019). Thus, the large-scale inward movement of TM9 reflects its substantial role in the conformational transitions of hENT1. In a word, the representative structure in hENT1_{dilazep} tends to a non-functional conformation located between the intermediate and outward occluded states of hENT1_{adenosine}, *i.e.*, outward occlusion blocked state.

The captured conformers can effectively depict the dynamic transition process of hENT1 from the outward open to occluded state after binding with adenosine. To quantitatively explore the transition details between different functional states, Fig. 9 shows the spatial variation of the potential transport channel from the outward open (empty) to occluded (adenosine-bound) state. When hENT1 is ready to bind the substrate in the outward open state, the entire extracellular transport channel is fully open (see Fig. 9A), and the maximum diameter point appears at the substrate binding site (see Fig. 9F). After binding adenosine, hENT1 goes through a transient intermediate state in which the extracellular thin gate rapidly narrows, but the transport channel diameter at the substrate binding site only drops by about 0.5 Å (see Fig. 9B and F). Subsequently, the extracellular thin gate is occluded to prevent the substrate from releasing into the extracellular side freely, and the

transport channel diameter at the substrate binding site shows a cliff-like decrease about 6 Å (see Fig. 9F). With the sequential induce-fit action between adenosine and the outward occluded hENT1 to form local complementary conformations, the extracellular side continues shrinking inwardly to transform into the occluded state. The intracellular thick gate always remains closed in all conformations, and it is clear that the real inward-facing state is not captured, possibly due to inadequate sampling.

By comparing the variation tendencies of channel diameter on the extracellular side, the outward occlusion blocked conformation of hENT1_{dilazep} is more similar to the unstable intermediate present in hENT1_{adenosine}. In this special conformation, the transport channel diameter at substrate binding site is still close to 6 Å. One of dilazep's trimethoxyphenyl rings occupies the opportunistic site to prevent the complete occlusion of thin gate, which not only disrupts the above local induce-fit action, but also blocks the conformational transitions of the whole protein, thus exhibiting distinct allosteric inhibition characteristics.

3.6. Molecular recognition between hENT1 and its ligands

Even though the rapid opening of the extracellular loop provides a dissociation channel for dilazep as we mentioned above, the previous experimental data has shown that the affinity of dilazep to hENT1 is much higher than that of adenosine (Huang et al., 2017; Vlachodimou

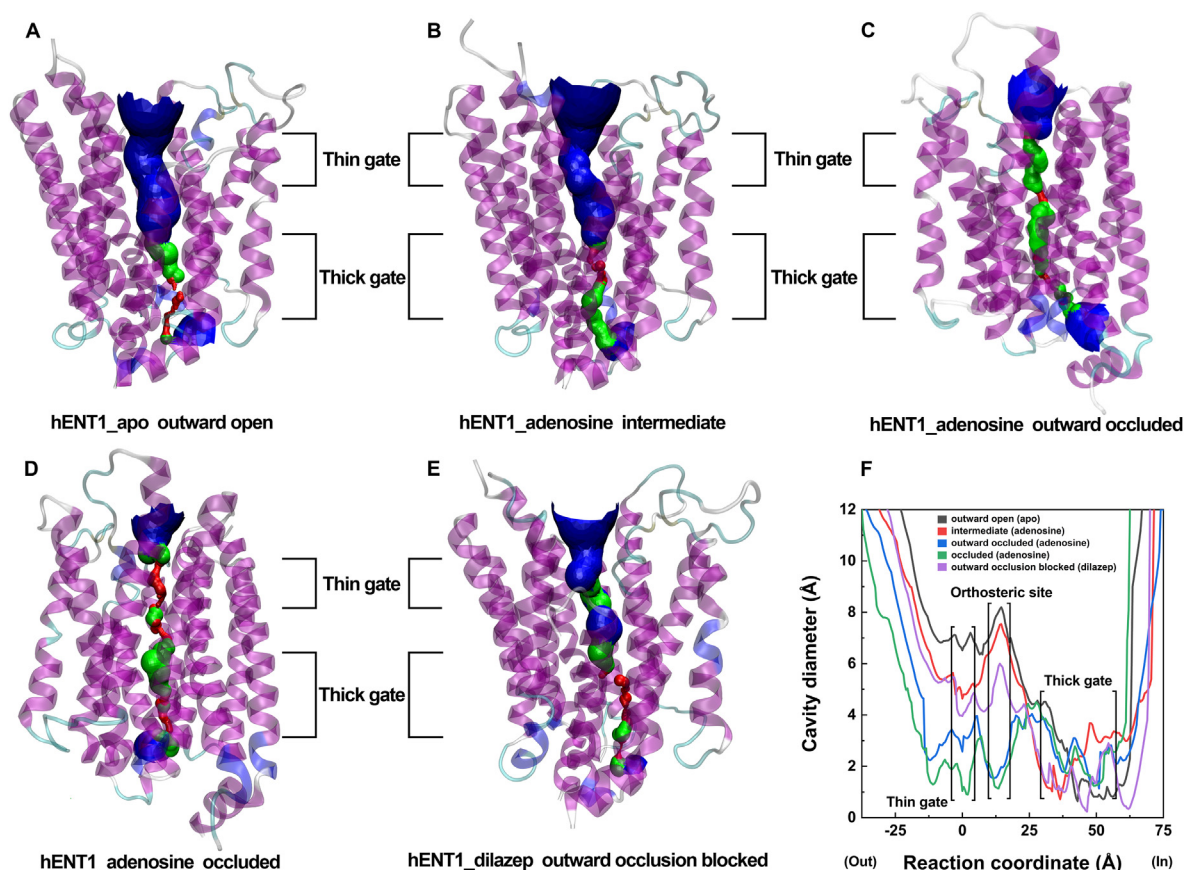


Fig. 9. Quantitative analysis of nucleoside transport channels based on different captured conformations in the hENT1_{apo} (A), hENT1_{adenosine} (B, C, D) and hENT1_{dilazep} (E) systems. Cavity diameter profiles versus distance along reaction coordinates in the three systems (F). The blue/green/red isosurfaces respectively represent the free/restricted/completely blocked substrate access areas, with cavity diameter greater than 5 Å/between 3 and 5 Å/less than 3 Å. The extracellular and cytosolic loops are not displayed for clarity. The channel diameter is determined by the maximum size of a probe sphere, and the calculated value may be smaller than the actual maximum diameter of cavity. (For interpretation of the references to color in this figure legend, the reader is referred to the Web version of this article.)

et al., 2020), suggesting a possible competitive inhibition mechanism. To further investigate molecular recognition of hENT1 by adenosine and dilazep, their binding free energies were predicted (see Fig. 10A).

The predicted binding free energies (-3.17 adenosine and -14.34 dilazep kcal \cdot mol $^{-1}$) agree well with experimental data (Huang et al., 2017; Vlachodimou et al., 2020) (-4.56 adenosine and -11.88 dilazep kcal \cdot mol $^{-1}$). For the hENT1_{adenosine} and hENT1_{dilazep} systems, electrostatic interaction energies (ΔELE) in the gas phase provide a beneficial contribution to the associations with adenosine and dilazep, but adverse solvation free energies (ΔGB) produce complete offset on this beneficial term. On the whole, polar interaction ($\Delta ELE + GB$) is not conducive to their binding. The entropy components ($-T\Delta S$) are also the detrimental factors weakening the binding strength of adenosine and dilazep to hENT1. ΔVDW and $\Delta GBSUR$, separately representing van der Waals interactions and nonpolar solvation energies, both provide beneficial hydrophobic contributions for ligand bindings. Specifically, the hydrophobic component ($\Delta VDW + GBSUR$) of the hENT1_{dilazep} system is greatly improved by 53.32 kcal mol $^{-1}$ relative to the hENT1_{adenosine} system. In terms of binding enthalpy (ΔH), hENT1_{dilazep} is 21.6 kcal mol $^{-1}$ higher than hENT1_{adenosine}. In summary, the binding free energy of dilazep to hENT1 is raised by 11.17 kcal mol $^{-1}$, showing a higher affinity than adenosine.

Obviously, VDW force plays a decisive role in the high affinity of dilazep, accounting for over 90% of hydrophobic contribution. To understand the essence behind the significant differences in VDW interactions between adenosine and dilazep with hENT1, both of their ΔVDW components were decomposed at the residue level. The obtained difference terms ($\Delta\Delta VDW_{\text{dilazep-adenosine}}$) can effectively identify the hot residues involved in VDW interactions. As shown in Fig. 10B, these hot

residues with $\Delta\Delta VDW$ value greater than -1 kcal mol $^{-1}$ include N30, M33, M84, P308, F334 and D341, which is almost consistent with the result of global binding energy decomposition (see Fig. S9). In fact, D341 is a negative-charged polar hydrophilic residue, which is unlikely to form strong VDW interactions with hENT1. The decomposed ΔVDW terms of D341 in hENT1_{dilazep} and hENT1_{adenosine} are a small negative and positive value, respectively. Therefore, the difference term of D341 can easily reach the setting threshold of -1 kcal mol $^{-1}$.

Subsequently, weak interaction analysis was performed to graphically reveal the detailed recognition mechanism of hENT1 hot residues with VDW interaction differences to adenosine and dilazep (see Fig. 10C and D). In Fig. 10C, the blue mixed with green isosurface between adenosine and D341 indicates that a strong charged H-bond is a key factor in their recognition (see the following analysis), conditionally tolerating an unfavorable positive value for the decomposed ΔVDW term of D341 in hENT1_{adenosine}. Apart from this, no other apparent weak interactions are found between adenosine and the hot residues. In Fig. 10D, extensive VDW interactions are formed between dilazep and the identified hot residues in the opportunistic site of hENT1. The large-area green isosurfaces between M33, F334 and the trimethoxyphenyl ring of dilazep represent classic pi-alkyl and pi-pi stacking interactions, respectively. There is another set of pi-alkyl interactions between M84, P308 and the diazepane linker of dilazep. Moreover, a weak neutral H-bond is formed between N30 and the methoxy group on trimethoxyphenyl ring, which is mainly driven by dispersion force and electrostatic interactions together (Emamian et al., 2019).

Electrostatic interaction plays a dominant role in the binding of adenosine, and the electrostatic component (ΔELE) of hENT1_{adenosine}

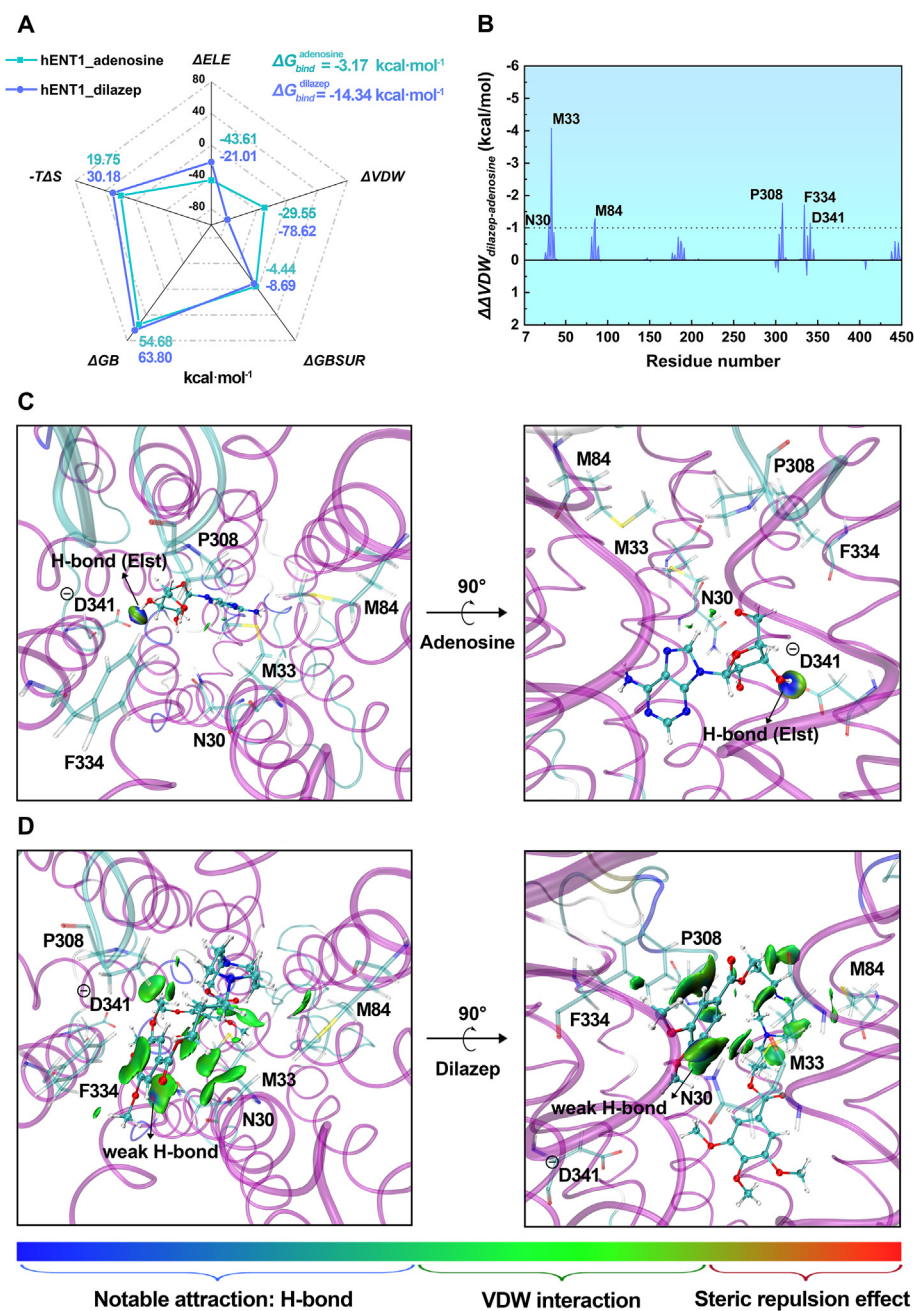


Fig. 10. Binding affinities of adenosine and dilazep to hENT1 calculated with MM-GBSA method (A). The ΔVDW difference value ($\Delta\Delta VDW$) of each residue between hENT1_dilazep and hENT1_adenosine (B). The weak interaction analysis using aIGM model at substrate binding cavities of hENT1_dilazep and hENT1_adenosine (C, D). Only the identified VDW hot residues are involved. Blue, green, and red are respectively used to describe strong attraction including charged hydrogen bonds, van der Waals force, as well as strong mutual exclusion including steric effect. The size of the isosurface determines the area where the interaction is formed. (For interpretation of the references to color in this figure legend, the reader is referred to the Web version of this article.)

is improved by $22.6 \text{ kcal}\cdot\text{mol}^{-1}$ relative to hENT1_dilazep (see Fig. 10A), although it doesn't reverse the affinity preference for hENT1 to dilazep. To elucidate molecular basis behind electrostatic interactions, the ΔELE components of hENT1_adenosine and hENT1_dilazep were decomposed into each residue. Q158, D341 and R345 are minded due to their $\Delta\Delta ELE$ values exceeding $-1 \text{ kcal}\cdot\text{mol}^{-1}$ (see Fig. S10A). The aIGM analysis reveals that adenosine and dilazep both can form a neutral H-bond with Q158 (see Figs. S10B and C). However, the blue isosurface between adenosine and Q158 suggests that this H-bond exhibits more polar electrostatic properties in the hENT1_adenosine system (see Figs. S10B and C). Consistent with previous electrostatic calculation, the strong electrostatically driven H-bond between adenosine and D341 can be corresponded to the large $\Delta\Delta ELE$ value over $-10 \text{ kcal}\cdot\text{mol}^{-1}$ (see Fig. 10C, S10A and S10B). Combined with the result of global binding energy decomposition (see Fig. S9), it can be inferred that D341 is a determining factor for the electrostatic association of adenosine. R345

not only participates in this extensive isosurface, but also forms an additional medium H-bond with the ribose hydroxyl of adenosine (see Fig. S10B). Notably, D341 and R345 have almost no interactions with dilazep.

To sum up, hENT1 prefers binding dilazep to adenosine, exhibiting a more negative binding free energy. The above aIGM analysis indicates that dilazep can form extensive and various VDW interactions with N30, M33, M84, P308 and F334 of hENT1 owing to the occupying effect of trimethoxyphenyl ring. It is the basis of stable interactions between dilazep and hENT1, as well as competitive inhibition mechanism.

4. Conclusion

To investigate dynamic structural features of hENT1 in adenosine transport and the inhibition mechanism of dilazep, three comparative

long-time unbiased MD simulations were performed. The key conformers in the transport cycle of hENT1 were captured by cluster analysis, revealing the dynamic transitions of hENT1 from the outward open to metastable occluded state mainly driven by TM1, TM2, TM7 and TM9. According to transport channel analysis, the sequential induce-fit action between adenosine and the outward occluded hENT1 results in a cliff-like decrease in the channel diameter at the substrate binding site, followed by further inward contraction of the extracellular side. One of the trimethoxyphenyl rings in dilazep serves as the adenosyl moiety of the endogenous adenosine substrate to competitively occupy the orthosteric site of hENT1, while the other is stuck in the opportunistic site near the extracellular side preventing the complete occlusion of thin gate simultaneously. Indeed, dilazep not only disrupts the local induce-fit action, but also blocks the transport cycle of the whole protein, thus exhibiting distinct allosteric inhibition characteristics.

The combined results of PCA, FEL and DCCM reveal a substrate-regulated gating strategy of extracellular loop, ensuring the endogenous substrate adenosine is firmly located in the transport cavity. Even though the rapid opening of the extracellular loop provides dilazep for a dissociation channel, the binding affinity of dilazep to hENT1 is still much higher than that of adenosine. From binding free energy calculations and weak interaction analyses, dilazep can form extensive and various VDW interactions with N30, M33, M84, P308 and F334 in hENT1 owing to the occupation effect of its trimethoxyphenyl ring. In a word, dilazep exerts its special hENT1 inhibitory function through competitive binding and allosteric regulation. Actually, cooperativity and induced fit are critical in molecular recognition and biological function. Our study indicates that the fragment-based ligand design strategy may be applicable to discover molecules with favorable properties that bind hENT1. The adenosine-mimicking fragment guides the inhibitor to bind firmly at the orthosteric site, and the sterically hindered fragment can block the conformational changes of hENT1 at the opportunistic site. Therefore, rational design of each individual fragment according to the different electrostatic and van der Waals environments and connecting them with an appropriate linker is the most critical step. This simulation not only provides nucleoside transport of hENT1 and the inhibition mechanisms of dilazep, but also supports the subsequent structure-based design of novel non-nucleoside AdoRIs.

CRedit authorship contribution statement

Zhixiang Wu: Conceptualization, Resources, Writing – original draft, Methodology. **Zhongjie Han:** Writing – review & editing. **Wenxue Zhou:** Methodology. **Xiaohan Sun:** Visualization. **Lei Chen:** Data curation. **Shuang Yang:** Data curation. **Jianping Hu:** Project administration, Supervision. **Chunhua Li:** Project administration, Supervision, Funding acquisition.

Declaration of competing interest

The authors declare the following financial interests/personal relationships which may be considered as potential competing interests: Chunhua Li reports financial support was provided by National Natural Science Foundation of China.

Acknowledgements

This work was supported by the National Natural Science Foundation of China (No. 31971180). We thank Yueteng Wang (Chengdu University) for his help in constructing the phylogenetic tree.

Appendix A. Supplementary data

Supplementary data to this article can be found online at <https://doi.org/10.1016/j.crstbi.2022.05.005>.

References

- Anandakrishnan, R., Aguilar, B., Onufriev, A.V., 2012. H++ 3.0: automating pK prediction and the preparation of biomolecular structures for atomic molecular modeling and simulations. *Nucleic Acids Res.* 40 (W1), W537–W541.
- Arastu-Kapur, S., Ford, E., Ullman, B., et al., 2003. Functional analysis of an inosine-guanosine transporter from *Leishmania donovani*: the role of conserved residues, aspartate 389 and arginine 393. *J. Biol. Chem.* 278, 33327–33333.
- Arastu-Kapur, S., Arendt, C.S., Purnat, T., et al., 2005. Second-site suppression of a nonfunctional mutation within the *Leishmania donovani* inosine-guanosine transporter. *J. Biol. Chem.* 280, 2213–2219.
- Asatryan, L., Nam, H.W., Lee, M.R., et al., 2011. Implication of the purinergic system in alcohol use disorders. *Alcohol Clin. Exp. Res.* 35, 584–594.
- Aseervatham, J., Tran, L., Machaca, K., et al., 2015. The role of flexible loops in folding, trafficking and activity of equilibrative nucleoside transporters. *PLoS One* 10, e0136779.
- Bayly, C.I., Cieplak, P., Cornell, W., et al., 1993. A well-behaved electrostatic potential based method using charge restraints for deriving atomic charges: the RESP model. *J. Phys. Chem.* 97, 10269–10280.
- Berendsen, H.J.C., Postma, J.P.M., van Gunsteren, W.F., et al., 1984. Molecular dynamics with coupling to an external bath. *J. Chem. Phys.* 81, 3684–3690.
- Bicket, A., Coe, I.R., 2016. N-linked glycosylation of N48 is required for equilibrative nucleoside transporter 1 (ENT1) function. *Biosci. Rep.* 36, e00376.
- Case, D.A., Belfon, K., Ben-Shalom, I.Y., et al., 2020. AMBER 2020. University of California, San Francisco.
- Deng, D., Sun, P., Yan, C., et al., 2015. Molecular basis of ligand recognition and transport by glucose transporters. *Nature* 526, 391–396.
- Dickson, C.J., Madej, B.D., Skjerveik Å, A., et al., 2014. Lipid14: the amber lipid force field. *J. Chem. Theor. Comput.* 10, 865–879.
- Downie, M.J., Kirk, K., Mamoun, C.B., 2008. Purine salvage pathways in the intraerythrocytic malaria parasite *Plasmodium falciparum*. *Eukaryot. Cell* 7, 1231–1237.
- Drew, D., Boudker, O., 2016. Shared molecular mechanisms of membrane transporters. *Annu. Rev. Biochem.* 85, 543–572.
- Drew, D., North, R.A., Nagarathinam, K., et al., 2021. Structures and general transport mechanisms by the major facilitator superfamily (MFS). *Chem. Rev.* 121, 5289–5335.
- Duan, H., Zhou, Y., Shi, X., et al., 2021. Allosteric and transport modulation of human concentrative nucleoside transporter 3 at the atomic scale. *Phys. Chem. Chem. Phys.* 23, 25401–25413.
- Emamian, S., Lu, T., Kruse, H., et al., 2019. Exploring nature and predicting strength of hydrogen bonds: a correlation analysis between atoms-in-molecules descriptors, binding energies, and energy components of symmetry-adapted perturbation theory. *J. Comput. Chem.* 40, 2868–2881.
- Engel, K., Zhou, M., Wang, J., 2004. Identification and characterization of a novel monoamine transporter in the human brain. *J. Biol. Chem.* 279, 50042–50049.
- Essmann, U., Perera, L., Berkowitz, M.L., et al., 1995. A smooth particle mesh Ewald method. *J. Chem. Phys.* 103, 8577–8593.
- Faham, S., Watanabe, A., Besserer, G.M., et al., 2008. The crystal structure of a sodium galactose transporter reveals mechanistic insights into Na⁺/sugar symport. *Science* 321, 810–814.
- Frisch, M.J., Trucks, G.W., Schlegel, H.B., et al., 2013. Gaussian 09, Revision D.01. Gaussian, Inc., Wallingford CT.
- Fukuda, M., Takeda, H., Kato, H.E., et al., 2015. Structural basis for dynamic mechanism of nitrate/nitrite antiport by NarK. *Nat. Commun.* 6, 7097.
- Genheden, S., Kuhn, O., Mikulskis, P., et al., 2012. The normal-mode entropy in the MM/GBSA method: effect of system truncation, buffer region, and dielectric constant. *J. Chem. Inf. Model.* 52, 2079–2088.
- Govindarajan, R., Bakken, A.H., Hudkins, K.L., et al., 2007. In situ hybridization and immunolocalization of concentrative and equilibrative nucleoside transporters in the human intestine, liver, kidneys, and placenta. *Am. J. Physiol. Regul. Integr. Comp. Physiol.* 293, R1809–R1822.
- Grein, J., Ohmagari, N., Shin, D., et al., 2020. Compassionate use of remdesivir for patients with severe Covid-19. *N. Engl. J. Med.* 382, 2327–2336.
- Griffiths, M., Beaumont, N., Yao, S.Y.M., et al., 1997. Cloning of a human nucleoside transporter implicated in the cellular uptake of adenosine and chemotherapeutic drugs. *Nat. Med.* 3, 89–93.
- Grimme, S., Antony, J., Ehrlich, S., et al., 2010. A consistent and accurate ab initio parametrization of density functional dispersion correction (DFT-D) for the 94 elements H-Pu. *J. Chem. Phys.* 132, 154104–154122.
- Hirsch, M., Johnson, Z.L., Lee, S.Y., 2017. Visualizing multistep elevator-like transitions of a nucleoside transporter. *Nature* 545, 66–70.
- Huang, W., Zeng, X., Shi, Y., et al., 2017. Functional characterization of human equilibrative nucleoside transporter 1. *Protein Cell* 8, 284–295.
- Humphrey, W., Dalke, A., Schulten, K., 1996. VMD: visual molecular dynamics. *J. Mol. Graph.* 14, 33–38.
- Ichiye, T., Karplus, M., 1991. Collective motions in proteins: a covariance analysis of atomic fluctuations in molecular dynamics and normal mode simulations. *Proteins: Struct. Inf. Bioinf.* 11, 205–217.
- Izaguirre, J.A., Catarello, D.P., Wozniak, J.M., et al., 2001. Langevin stabilization of molecular dynamics. *J. Chem. Phys.* 114, 2090–2098.
- Jardetzky, O., 1966. Simple allosteric model for membrane pumps. *Nature* 211, 969–970.
- Jo, S., Lim, J.B., Klauda, J.B., et al., 2009. CHARMM-GUI Membrane Builder for mixed bilayers and its application to yeast membranes. *Biophys. J.* 97, 50–58.
- Jorgensen, W.L., Chandrasekhar, J., Madura, J.D., et al., 1983. Comparison of simple potential functions for simulating liquid water. *J. Chem. Phys.* 79, 926–935.

- Krishnamurthy, H., Piscitelli, C.L., Gouaux, E., 2009. Unlocking the molecular secrets of sodium-coupled transporters. *Nature* 459, 347–355.
- Lane, A.N., Fan, T.W.M., 2015. Regulation of mammalian nucleotide metabolism and biosynthesis. *Nucleic Acids Res.* 43, 2466–2485.
- Lefebvre, C., Rubez, G., Khartabil, H., et al., 2017. Accurately extracting the signature of intermolecular interactions present in the NCI plot of the reduced density gradient versus electron density. *Phys. Chem. Chem. Phys.* 19, 17928–17936.
- Lindberg, D., Shan, D., Ayers-Ringler, J., et al., 2015. Purinergic signaling and energy homeostasis in psychiatric disorders. *Curr. Mol. Med.* 15, 275–295.
- Lu, T., Chen, F., 2012. Multiwfn: a multifunctional wavefunction analyzer. *J. Comput. Chem.* 33, 580–592.
- Maier, J.A., Martinez, C., Kasavajhala, K., et al., 2015. ff14SB: improving the accuracy of protein side chain and backbone parameters for ff99SB. *J. Chem. Theor. Comput.* 11, 3696–3713.
- Maisuradze, G.G., Liwo, A., Scheraga, H.A., 2010. Relation between free energy landscapes of proteins and dynamics. *J. Chem. Theor. Comput.* 6, 583–595.
- Mayo, S.L., Olafson, B.D., Goddard, W.A., 1990. DREIDING: a generic force field for molecular simulations. *J. Phys. Chem.* 94, 8897–8909.
- McLean, A.D., Chandler, G.S., 1980. Contracted Gaussian basis sets for molecular calculations. I. Second row atoms, $Z=11-18$. *J. Chem. Phys.* 72, 5639–5648.
- Mitchell, P., 1957. A general theory of membrane transport from studies of bacteria. *Nature* 180, 134–136.
- Molina-Arcas, M., Casado, F.J., Pastor-Anglada, M., 2009. Nucleoside transporter proteins. *Curr. Vasc. Pharmacol.* 7, 426–434.
- Nam, H.W., McIver, S.R., Hinton, D.J., et al., 2012. Adenosine and glutamate signaling in neuron-glia interactions: implications in alcoholism and sleep disorders. *Alcohol Clin. Exp. Res.* 36, 1117–1125.
- Nam, H.W., Bruner, R.C., Choi, D.S., 2013. Adenosine signaling in striatal circuits and alcohol use disorders. *Mol. Cell.* 36, 195–202.
- Nomura, N., Verdon, G., Kang, H.J., et al., 2015. Structure and mechanism of the mammalian fructose transporter GLUT5. *Nature* 526, 397–401.
- Onufriev, A., Bashford, D., Case, D.A., 2004. Exploring protein native states and large-scale conformational changes with a modified generalized born model. *Proteins: Struct. Inf. Bioinf.* 55, 383–394.
- Quistgaard, E.M., Löw, C., Guettou, F., et al., 2016. Understanding transport by the major facilitator superfamily (MFS): structures pave the way. *Nat. Rev. Mol. Cell Biol.* 17, 123–132.
- Qureshi, A.A., Suades, A., Matsuoka, R., et al., 2020. The molecular basis for sugar import in malaria parasites. *Nature* 578, 321–325.
- Roe, D.R., Cheatham III, T.E., 2013. PTRAJ and CPPTRAJ: software for processing and analysis of molecular dynamics trajectory data. *J. Chem. Theor. Comput.* 9, 3084–3095.
- Ruby C. L., Adams C. A., Knight E. J., et al., 2010. An essential role for adenosine signaling in alcohol abuse. *Curr. Drug Abuse Rev.* 3, 163–174.
- Ryckaert, J.P., Ciccotti, G., Berendsen, H.J.C., 1977. Numerical integration of the cartesian equations of motion of a system with constraints: molecular dynamics of n-alkanes. *J. Comput. Phys.* 23, 327–341.
- Seley-Radtke, K.L., Yates, M.K., 2018. The evolution of nucleoside analogue antivirals: a review for chemists and non-chemists. Part I: early structural modifications to the nucleoside scaffold. *Antivir. Res.* 154, 66–86.
- Sheahan, T.P., Sims, A.C., Zhou, S., et al., 2020. An orally bioavailable broad-spectrum antiviral inhibits SARS-CoV-2 in human airway epithelial cell cultures and multiple coronaviruses in mice. *Sci. Transl. Med.* 12, eabb5883.
- Sun, H., Li, Y., Shen, M., et al., 2014a. Assessing the performance of MM/PBSA and MM/GBSA methods. 5. Improved docking performance using high solute dielectric constant MM/GBSA and MM/PBSA rescoring. *Phys. Chem. Chem. Phys.* 16, 22035–22045.
- Sun, H., Li, Y., Tian, S., et al., 2014b. Assessing the performance of MM/PBSA and MM/GBSA methods. 4. Accuracies of MM/PBSA and MM/GBSA methodologies evaluated by various simulation protocols using PDBbind data set. *Phys. Chem. Chem. Phys.* 16, 16719–16729.
- Sundaram, M., Yao, S.Y.M., Ingram, J.C., et al., 2001. Topology of a human equilibrative, nitrobenzylthioinosine (NBMPR)-sensitive nucleoside transporter (hENT1) implicated in the cellular uptake of adenosine and anti-cancer drugs. *J. Biol. Chem.* 276, 45270–45275.
- Trott, O., Olson, A.J., 2010. AutoDock Vina: improving the speed and accuracy of docking with a new scoring function, efficient optimization, and multithreading. *J. Comput. Chem.* 31, 455–461.
- Van Rompay, A.R., Johansson, M., Karlsson, A., 2000. Phosphorylation of nucleosides and nucleoside analogs by mammalian nucleoside monophosphate kinases. *Pharmacol. Therapeut.* 87, 189–198.
- Vlachodimou, A., Konstantinopoulou, K., IJzerman, A.P., et al., 2020. Affinity, binding kinetics and functional characterization of drafazine analogues for human equilibrative nucleoside transporter 1 (SLC29A1). *Biochem. Pharmacol.* 172, 113747.
- Wang, J., Wolf, R.M., Caldwell, J.W., et al., 2004. Development and testing of a general amber force field. *J. Comput. Chem.* 25, 1157–1174.
- Wang, M., Cao, R., Zhang, L., et al., 2020. Remdesivir and chloroquine effectively inhibit the recently emerged novel coronavirus (2019-nCoV) in vitro. *Cell Res.* 30, 269–271.
- Ward, J.L., Sherali, A., Mo, Z.P., et al., 2000. Kinetic and pharmacological properties of cloned human equilibrative nucleoside transporters, ENT1 and ENT2, stably expressed in nucleoside transporter-deficient PK15 cells: ENT2 exhibits a low affinity for guanosine and cytidine but a high affinity for inosine. *J. Biol. Chem.* 275 (12), 8375–8381.
- Waterhouse, A., Bertoni, M., Bienert, S., et al., 2018. SWISS-MODEL: homology modelling of protein structures and complexes. *Nucleic Acids Res.* 46, W296–W303.
- Weyand, S., Shimamura, T., Yajima, S., et al., 2008. Structure and molecular mechanism of a nucleobase-cation-symport-1 family transporter. *Science* 322, 709–713.
- Wright, N.J., Lee, S.Y., 2019. Structures of human ENT1 in complex with adenosine reuptake inhibitors. *Nat. Struct. Mol. Biol.* 26, 599–606.
- Wright, N.J., Lee, S.Y., 2020. Toward a molecular basis of cellular nucleoside transport in humans. *Chem. Rev.* 121, 5336–5358.
- Wu, Z., Peng, L., Hu, Y., et al., 2020. BP[dG]-induced distortions to DNA polymerase and DNA duplex: a detailed mechanism of BP adducts blocking replication. *Food Chem. Toxicol.* 140, 111325.
- Wu, Z., Duan, H., Cheng, Y., et al., 2022. A novel ligand swing-mediated active site coordination change of human apurinic/apyrimidinic endonuclease 1: a potential cytotoxic mechanism of nickel ion in the base excision repair. *Chem. Phys.* 555, 111456.
- Yamashita, A., Singh, S.K., Kawate, T., et al., 2005. Crystal structure of a bacterial homologue of Na⁺/Cl⁻-dependent neurotransmitter transporters. *Nature* 437, 215–223.
- Yao, S.Y.M., Ng, A.M.L., Cass, C.E., et al., 2011. Nucleobase transport by human equilibrative nucleoside transporter 1 (hENT1). *J. Biol. Chem.* 286, 32552–32562.
- Yates, M.K., Seley-Radtke, K.L., 2019. The evolution of antiviral nucleoside analogues: a review for chemists and non-chemists. Part II: complex modifications to the nucleoside scaffold. *Antivir. Res.* 162, 5–21.
- Yegutkin, G.G., 2014. Enzymes involved in metabolism of extracellular nucleotides and nucleosides: functional implications and measurement of activities. *Crit. Rev. Biochem. Mol. Biol.* 49, 473–497.
- Yin, Y., He, X., Szewczyk, P., et al., 2006. Structure of the multidrug transporter EmrD from *Escherichia coli*. *Science* 312, 741–744.
- Young, J.D., Yao, S.Y.M., Sun, L., et al., 2008. Human equilibrative nucleoside transporter (ENT) family of nucleoside and nucleobase transporter proteins. *Xenobiotica* 38, 995–1021.
- Young, J.D., Yao, S.Y.M., Baldwin, J.M., et al., 2013. The human concentrative and equilibrative nucleoside transporter families, SLC28 and SLC29. *Mol. Aspect. Med.* 34, 529–547.
- Zhang, M., Hao, Q., 2011. Crystal structure of NDM-1 reveals a common β -lactam hydrolysis mechanism. *Faseb. J.* 25, 2574–2582.